# Inhibition grain growth and electrical properties by adding $In_2O_3$ to $SnO_2$-$Co_3O_4$-$Ta_2O_5$ ceramics

M. Olvera-Sánchez[a], M.B. Hernández[a,e], S. García-Villarreal[b], E. Rodríguez[a], C. Gómez Rodríguez[c], L.V. Garcia-Quiñonez[d] and J.A. Aguilar-Martínez[a,*]

[a] *Universidad Autónoma de Nuevo León, Facultad de Ingeniería Mecánica y Eléctrica, Centro de Investigación e Innovación en Ingeniería Aeronáutica (CIIIA); Carretera a Salinas Victoria km. 2.3, C.P. 66600, Apodaca, N.L., México.*

**e-mail: josue.aguilar74@gmail.com; josue.aguilarmrt@uanl.edu.mx*

[b] *Universidad Autónoma de Coahuila, Facultad de Metalurgia, Carr. 57, Km 4.5, C.P. 25710, Monclova, Coah., México.*

[c] *Universidad Politécnica de Apodaca (UPAP); Av. Politécnica cruz con la carretera Miguel Alemán, km 24.5, 66600 Apodaca, N.L., México.*

[d] *Universidad Politécnica de García; Calle Porfirio Díaz No. 106, Col. Centro Villa de García, 66000 García, N.L., México.*

[e] *Tecnológico de Monterrey, Centro de Innovación y Diseño en Tecnología. Av. Eugenio Garza Sada 2501, C.P. 64849, Monterrey, N. L., México*

Received 31 August 2018; accepted 20 September 2018

In this contribution, the effect of $In_2O_3$ additions on the microstructure, physical and electrical properties of the $SnO_2$-$Co_3O_4$-$Ta_2O_5$ ceramic system was investigated. Because the effect of $In_2O_3$ has been studied typically at low levels, special attention has been paid to the effect of high levels (1 and 2 mol % $In_2O_3$) in the ceramics. Results show that up to 0.1 mol % $In_2O_3$, an increase of indium oxide content is correlated with grain size reduction and an increase of the nonlinearity coefficient ($\alpha$) and breakdown voltage ($E_B$), producing an augmentation by a factor of 2 in the nonlinearity coefficient and an increment by a factor of 8 in the breakdown voltage. However, shrinkage ($\gamma$) and measured density are not influenced by the addition of indium oxide. For samples with 1 and 2 mol % $In_2O_3$, in non-calcined condition, $In_2O_3$ is present with cubic structure. However, in calcined specimens, $In_2O_3$ is not detected anymore and $SnO_2$-crystal structure undergoes a change from tetragonal to cubic. These ceramic samples exhibit high resistivity, behaving like dielectric materials.

*Keywords:* Electrical properties; varistors; sintering; grain boundaries; breakdown voltage.

PACS: 81.20.Ev; 61.05.cp; 84.32.Ff.

## 1. Introduction

The most important role of solid-state electronic ceramic components known as varistors (nonlinear resistors) is to sense and limit transient voltage surges. For this reason, they have been extensively used to protect electronic equipment from overvoltage [1]. Varistors are characterized with respect to other devices by two essential aspects, namely: i) symmetry (the same value at different voltage polarities) and nonlinearity (the resistance decreases with the applied voltage) [2]. The current-voltage ($j(E)$) characteristic of a varistor is usually calculated using the equation $j = kE^{\alpha}$, where $j$ is the current density, $E$ is the electrical field, $\alpha$ is the nonlinear electrical coefficient, and $k$ is a constant related to the material microstructure [3]. The greater the value of $\alpha$, the better the device to protect an equipment.

Tin dioxide ($SnO_2$) is an n-type semiconductor with a wide direct band gap of 3.6 eV at 300 K [4], with a rutile-type structure and space group $D_{4h}^{14}$ [5]. In the absence of additives during sintering, tin dioxide has poor densification characteristics. For this reason it has found applications as moisture and gas sensor devices [4,6]. However, the preparation of $SnO_2$- based ceramics with high density, makes of tin dioxide a prominent material for use in other important electronic applications such as varistors [7-9]. High dense tin dioxide ceramics can be attained either by the introduction of densifying agents, such as CuO [10], ZnO [11], $Co_3O_4$ [12], and $MnO_2$ [13], or by use of adequate fabrication techniques, like hot isostatic pressure processing [14], which promotes densification of $SnO_2$ almost to the theoretical density value.

The effect of $In_2O_3$ content on the microstructure and electrical properties of $SnO_2$-based varistors has been investigated previously by different authors, doping the ceramics with Co-Ta [15] and with Co-Nb [16]. Despite the difference in the second dopant (Ta or Nb), in both studies it was concluded that variations of electrical properties are attributed mainly to variations of grain size. However, and more specifically, in addition to variations of grain size, in the case of Co-Ta doped samples, the variations in electrical properties are also attributed to resistivity of grain boundaries, whilst in the case for Co- Nb samples, the increase of breakdown electrical field with increase in $In_2O_3$ content is ascribed only to the decrease of grain size. Taking everything into account, it is apparent that the use of Ta is promising for attaining a higher non-linear coefficient ($\alpha$).

Whilst the prior investigations have focused mainly on studying the effect of low and medium levels of additions of $In_2O_3$, to the best of the author's knowledge, no previous work has reported results from the effect of high levels of addition of $In_2O_3$ to $SnO_2$-based ceramics. Preliminary work by the authors suggests that high quantities of addition of $In_2O_3$ impact significantly the grain size in the microstructure of the ceramics. On that context, the aim of this work was to investigate the effect of $In_2O_3$ additions - emphasizing on high addition levels - on the microstructure, physical and electrical properties of $SnO_2$-$Co_3O_4$-$Ta_2O_5$ ceramics.

## 2. Materials and methods

Analytical-grade $SnO_2$ (Aldrich), $Co_3O_4$ (Aldrich), $In_2O_3$ (Aldrich) and $Ta_2O_5$ (Aldrich) powders were used as the starting materials for sample preparation. The molar composition of the investigated systems was (98.95-X) % $SnO_2$-1 % $Co_3O_4$-0.05 % $Ta_2O_5$-X % $In_2O_3$, where X = 0.0, 0.05, 0.1, 1 and 2%. The powders were mixed through high-energy milling performed for 20 minutes in a planetary ball-mill (Pulverisette 7, Fritsch GmbH) using vials and balls of agate. The resulting powders were uniaxially pressed in the form of tablets (0.9 mm in diameter) at 230 MPa without the use of binders.

The tablets were sintered in a tube furnace (Nabertherm RHTH 120/300/1700). Maximum sintering temperature was 1350°C for 1 h. The sintering cycle is fully described in Fig. 1. Both ends of the tube furnace were capped with ceramic fiber. After cooling down to room temperature, the samples were removed from the furnace to be prepared for characterization. The density of the sintered samples was determined by Archimedes' method and the linear shrinkage $\gamma$ was calculated according to the expression:

$$\gamma = \frac{D_0 - D}{D_0} \tag{1}$$

where $D_0$ and $D$ are diameters of the sample before and after sintering, respectively.

All ceramic systems of the present study were characterized by means of thermal analysis in the range of 30 to 1500°C in a simultaneous TG-DSC-DTA equipment (TA-Instruments model SDT Q600). Samples of 20 to 30 mg were placed in the thermal analyzer within a platinum crucible and heated at the rate of 10°C/min in static air, using alumina as reference material. The temperature range was established in order to corroborate the occurrence of the spinel phase $Co_2SnO_4$ in the temperature range, as reported previously [17]. All samples were analyzed under the same thermal conditions.

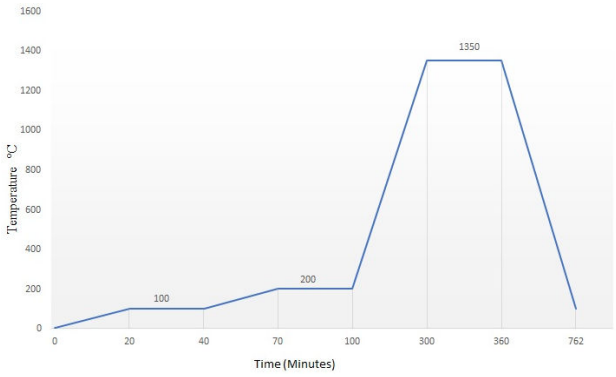


FIGURE 1. Sintering thermal cycle used for all samples.

The determination of phases was conducted by X-ray diffraction technique (XRD; PANalytical Empyrean model) with CuK$\alpha$ radiation ($\lambda = 1.5406$ Å) operated at 45 kV, 40 mA and a Pixel 1D detector in Bragg-Brentano geometry. The scans were performed in the $2\theta$ range from 10 to 100° with a step scan of 0.016° and 20 s per step in a continuous mode. Phase identification was performed with X'Pert HighScore Plus software, version 4.6, and the ICDD PDF-4 plus database (ICDD International Center for Diffraction Data, Newtown Square, PA). The microstructure of the samples was characterized by scanning electron microscopy (SEM; model Nova Nano SEM 200, FEI). The mean grain size was determined from SEM micrographs with the aid of an image analysis software (Image-Pro Plus), according to the ASTM-E112 standard procedures.

For electrical characterization, equal silver electrodes were placed on both faces of the sintered ceramic specimens. Current-voltage measurements were conducted using a High Voltage Measure Unit (Keithley 2410). The nonlinear coefficient $\alpha$ was determined at a current density of 1-10 mAcm$^{-2}$ using the following equation:

$$\alpha = \frac{\log(J_2/J_1)}{\log(E_2/E_1)} \tag{2}$$

where $E_1$ and $E_2$ are the applied electric fields corresponding to the current densities $J_1 = 1$ mAcm$^{-2}$ and $J_2 = 10$ mAcm$^{-2}$, respectively. The breakdown voltage $E_B$ was measured at 1 mAcm$^{-2}$. $J$ and $E$ can be calculated by means of $i/s$ and $V/t$, where $i$ is the electric current, $s$ is the area of silver electrode and $t$ is the thickness of the tested sample.

## 3. Results and discussion

Figure 2 shows representative SEM photomicrographs of all specimens taken at the same magnification for comparison purposes, from the specimen with 0 % $In_2O_3$ (Fig. 2a) to that with 2 mol % $In_2O_3$ (Fig. 2e).

Although there is no manifest appearance of equiaxed grains - particularly for specimens with 0.1 and 1 mol % $In_2O_3$ (Figs, 2c and 2d, respectively) -, there is, however a tendency in grain size reduction, markedly observed in the specimen with the highest level of In2O3 (2 mol %, Fig. 2e). The mean grain size ($l_g$) of specimens prepared with all compositions is reported in Table I, showing that at the highest level of $In_2O_3$ (2 mol %), a grain reduction of about 43 % is reached, compared with the specimen without $In_2O_3$ addition. Despite the observed grain size reduction, shrinkage

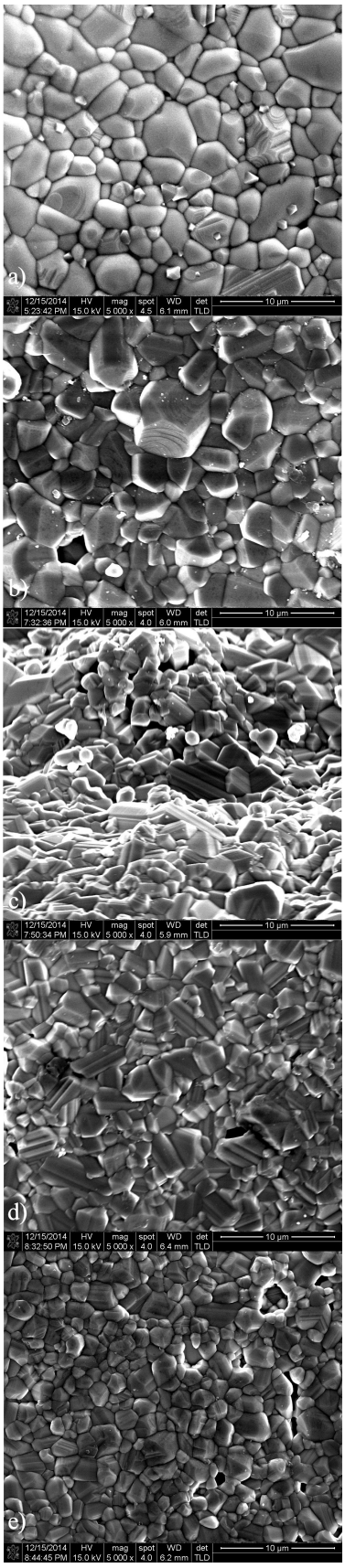


FIGURE 2. SEM micrographs of samples sintered at 1350°C for 1 hour: (a) 0.00, (b) 0.05, (c) 0.1, (d) 1 and (e) 2 % $In_2O_3$.

($\gamma$) does not seem to be influenced by the addition of indium oxide, being also the case for the measured density. The magnitudes of density, relative density, grain size and shrinkage are all summarized in Table I.

Representative X-ray powder diffraction patterns of non-calcined and calcined samples are shown in Fig. 3. For non-calcined samples doped with 0.0, 0.05 and 0.1 mol% (Fig. 3a), the identified peaks correspond to $Co_3O_4$ with cubic structure (ICDD PDF # 04-003-0984) and $SnO_2$ with tetragonal structure (ICDD PDF # 04-005-5929), while in the case of doped samples with 1 and 2 mol %, the presence of the above mentioned phases was observed, together with $In_2O_3$, with cubic structure (ICDD PDF # 04-008-2461) (marked as $\bullet$, $*$, $\circ$, respectively), suggesting an excess of $In_2O_3$ in those samples. XRD patterns from samples 0.05 and 0.1 mol% show no evidence of $In_2O_3$ since the content of this oxide is below the limit of detection of the equipment. In the case of calcined samples (Fig. 3b), $SnO_2$ (tetragonal) still prevails common to all compositions, but the reactants $Co_3O_4$ and $In_2O_3$ are not present anymore, at least within the detection limits of the equipment. Moreover, for calcined specimens with 1 and 2 mol%, the presence of $SnO_2$ with cubic structure, is observed (ICDD PDF # 00-033-1374). Since the solubility of $In_2O_3$ in $SnO_2$ has been reported [18] to be about 96.1-94.4 mol % $SnO_2$ (3.9-5.6 mol % $In_2O_3$), and as

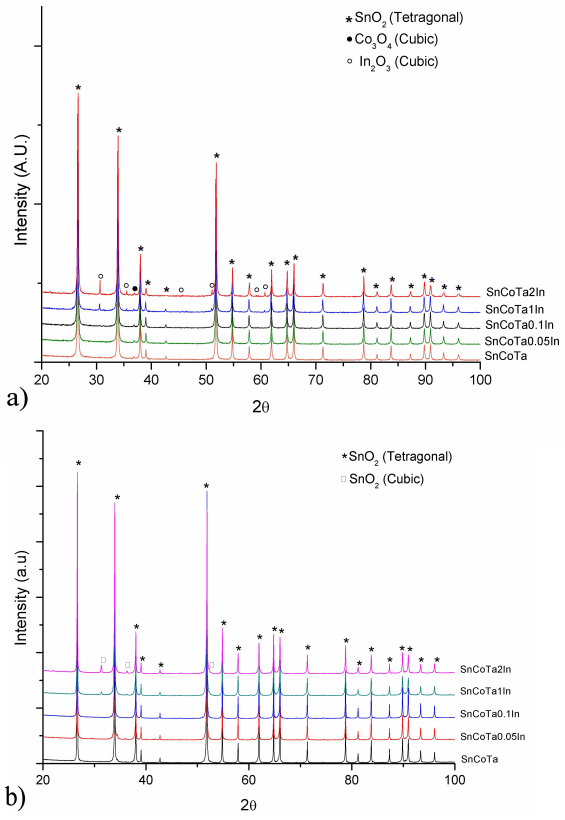


FIGURE 3. XRD patterns of $SnO_2$ ceramics with different indium oxide contents: (a) for non-calcined samples and (b) calcined samples.

TABLE I. Shrinkage ($\gamma$), measured density ($\rho$), relative theoretical density ($\rho_{tr}$), mean grain size ($l_g$), nonlinearity coefficient ($\alpha$) and electric field at fixed current density ($E_1$) of the samples doped with different contents of $In_2O_3$.

| $In_2O_3$ (mol %) | $\gamma$ (%) | $\rho$ (g/cm$^3$) | $^{\alpha}\rho_{tr}$ (%) | $l_g$ ($\mu$m) | $\alpha$ | $E_B$ (V/cm) |
|---|---|---|---|---|---|---|
| 0.00 | 10.87 | 6.61 | 95.43 | 2.1 | 10.72 | 1551.40 |
| 0.05 | 11.07 | 6.57 | 94.87 | 2.20 | 10.80 | 2053.44 |
| 0.1 | 11.18 | 6.60 | 95.30 | 1.89 | — | — |
| 1 | 10.58 | 6.47 | 93.34 | 1.44 | — | — |
| 2 | 11.03 | 6.31 | 91.00 | 1.24 | — | — |

[a] Theoretical density of $SnO_2$ is 6.95 g/cm$^3$.

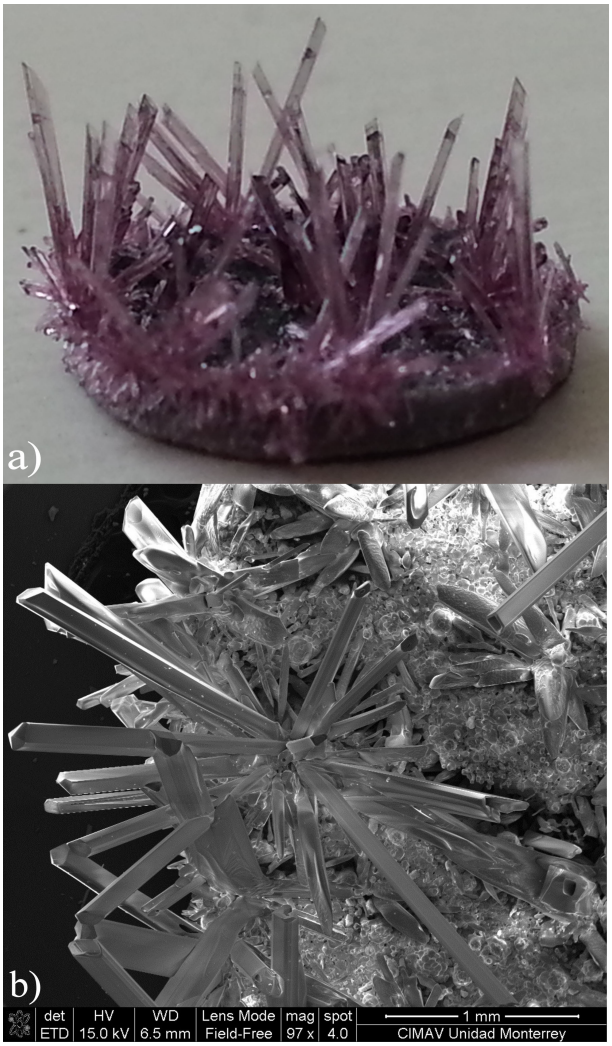


FIGURE 4. Photograph showing crystal formation on the surface of ceramic sample (a). SEM micrograph displays detailed hollow needle-like shape of crystals (b).

no free $In_2O_3$ was identified by the diffractometer, the authors suggest that indium oxide was incorporated into the $SnO_2$ lattice modifying its crystal structure from tetragonal to cubic. Although the spinel phase $Co_2SnO_4$ is not detected by conventional XRD analysis, analysis by DTA/TGA reveals an endothermic peak at 920°C, which in accord to previous works by the same research group, corresponds to spinel formation [17,19].

Figure 4a shows what appears to be a habitus of $SnO_2$ single crystals formed during sintering on the surface of samples. The color of these crystals went from pale pink to purple as the $In_2O_3$ content increased. Crystals with hollow needle-like shape are observed at high magnification (Fig. 4b). The surface crystals formed during sintering were analyzed by XRD. A set of diffraction patterns are shown in Fig. 5. First, a crystal was carefully removed from the surface of the ceramic disc and placed in a zero background holder. The resulting pattern is labeled as Setting 1. Then, the sample holder with the sample on it was rotated by 90° with respect to the previous setting. The resulting pattern is presented as Setting 2. Finally, the crystal was powdered in an agate mortar. The corresponding XRD pattern is labeled as Powdered Crystal. Identified peaks correspond to tetragonal $SnO_2$ (ICDD PDF # 4 01-072-1147); according to this card, and following the intensity order, the three most intense diffraction planes were identified and indexed. The difference in intensity is relate to preferential crystallographic orientation. Authors suggest the high content of $In_2O_3$ had a noticeable effect for the occurring of the formation of $SnO_2$ habitus on the surface of samples since at lower contents this outcome had not been previously reported.

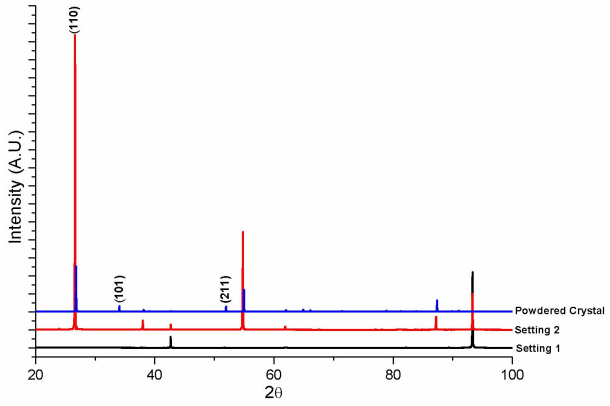


FIGURE 5. Diffraction patterns of a crystal taken from the surface of sample showing preferred orientation.

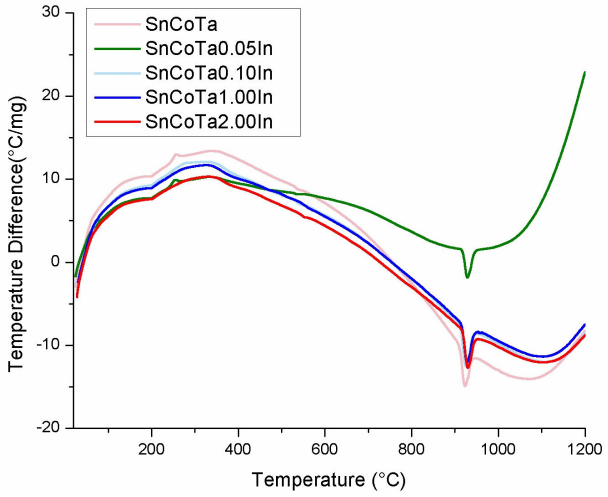


FIGURE 6. DSC curves of the decomposition of (a) 0.00, (b) 0.05, (c) 0.1, (d) 1 and (e) 2 % $In_2O_3$.

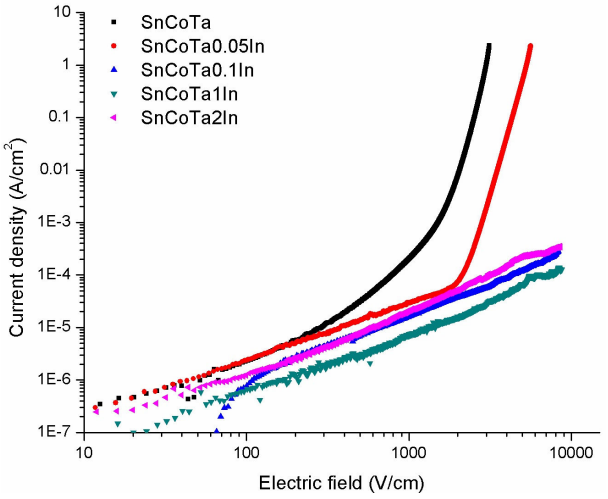


FIGURE 7. $J-E$ characteristic plots of sintered samples.

Results from the differential thermal analyses for all compositions before sintering are shown in Fig. 6. The thermograms indicate the presence of a main endothermic peak associated to the spinel ($Co_2SnO_4$) formation at the temperature of 920°C. At high temperatures, $Co_3O_4$ decomposes into CoO as reaction product, following the reaction equation:

$$2Co_3O_4 \xrightarrow{850^\circ C} 6Co\,O + O_2 \qquad (3)$$

Once the CoO is obtained, and since $SnO_2$ is present, then the formation of the spinel phase follows the reaction given by:

$$2CoO + Sn\,O_2 \xrightarrow{920^\circ C} Co_2 + Sn\,O_4 \qquad (4)$$

Details on the formation mechanism of the $Co_2SnO_4$ phase detected by DTA/TGA are reported elsewhere [17,19].

The reason why specimens with 1 and 2 % $In_2O_3$ does not reveal formation of the spinel phase $In_4Sn_3O_{12}$ is found on the related literature, since published reports state that the spinel formation is reached at higher temperatures than those used for sintering in the current investigation [20,21].

Results from electrical ($J-E$) measurements for the set of specimens with all experimental compositions and for reference materials, are shown in Fig. 7. As can be seen in this figure, only the reference material and the specimen with 0.05 mol. % $In_2O_3$ exhibited non-linear or varistor behavior. Apparently, above 0.05 mol % $InO_2$, the specimens show a highly resistive performance, behaving like dielectric materials. This tendency can be observed in the values of measured mean grain size ($l_g$) shown in column 5 of Table I. Therefore, it can be stated that as the $In_2O_3$ content increases there is a decrease in grain size and an increase in the breakdown voltage.

## 4. Conclusions

In this work the effect of $In_2O_3$ additions on the microstructure, physical and electrical properties of the $SnO_2$-$Co_3O_4$-$Ta_2O_5$ ceramic system was investigated. Because the effect of $In_2O_3$ has been studied typically at low levels, special attention has been paid to the effect of high levels (1 and 2 mol % $In_2O_3$) in the ceramics. Results show that up to 0.1 mol % $In_2O_3$, an increase of indium oxide content is correlated with grain size reduction and an increase of the nonlinearity coefficient ($\alpha$) and breakdown voltage ($E_B$), producing an augmentation by a factor of 2 in the nonlinearity coefficient and an increment by a factor of 8 in the breakdown voltage. For $In_2O_3$ contents above 0.05 % mol the ceramic samples behave like dielectrics. Additionally, a high content of $In_2O_3$ may be responsible of promoting the formation of a $SnO_2$ habitus on the surface of samples.

## Acknowledgments

This study was supported by the National Science and Technology Council of Mexico (CONACYT) under the project "Convocatoria Ciencia Basica 2014 (project number 238054)". M. Olvera-Sánchez also thanks the CONACyT, México for his postgraduate scholarship.

1. T.K. Gupta, *J. Am. Ceram. Soc*. **73** (1990) 1817.
2. J.A. Aguilar-Martínez, E. Rodríguez, S. García-Villarreal, L. Falcon-Franco and M.B. Hernández, *Mater. Chem. Phys*. **153** (2015) 180.
3. L.M. Levinson and H.R. Philipp, *J. Appl. Phys*. *46* (1975) 1332.
4. Y. Zhao, J. Liu, Q. Liu, Y. Sun, D. Song, W. Yang, J. Wang and L. Liu, *Mater. Lett*. **136** (2014) 286.
5. S. Das and V. Jayaraman, *Prog. Mater. Sci*. **66** (2014) 112.
6. E.M. El-Maghraby, A. Qurashi and T. Yamazaki, *Ceram. Int*. **39** (2013) 8475.
7. G.-Z. Zang, X.-F. Wang, L.-B. Li and D.-D. Wang, *Ceram. Int*. **43** (2017) 8018.
8. N. Yongvanich, K. Niyomtrum, C. Chairatanaset and T. Srisethkul, *Ceram. Int*. **43** (2017) S280.
9. M.M. Shahraki, M. Golmohammad, I. Safaee and M.D. Chermahini, *Ceram. Int.* **44** (2018) 3388.
10. T.S. Zhang, L.B. Kong, X.C. Song, Z.H. Du, W.Q. Xu and S. Li, *Acta Mater.* **62** (2014) 81.
11. J. He, Z. Peng, Z. Fu, C. Wang and X. Fu, *J. Alloy. Compd.* **528** (2012) 79.
12. J.A. Aguilar-Martínez, M.I. Pech-Canul, C. Leyva-Porras, E. Rodríguez and V. Iván Hernández, *Ceram. Int.* **39** (2013) 8237.
13. E.N.S. Muccillo and R. Muccillo, *J. Eur. Ceram. Soc*. **34** (2014) 3699.
14. K. Uematsu, Z. Kato, N. Uchida and K. Saito, *J. Am. Ceram. Soc*. **70** (1987) C.
15. G.Z. Zang, J.F. Wang, H.C. Chen, W.B. Su, W.X. Wang, C.M. Wang and P. Qi, *J. Non-Cryst. Solids.* **351** (2005) 941.
16. W.X. Wang, J.F. Wang, H.C. Chen, W.B. Su, B. Jiang, G.Z. Zang, C.M. Wang and P. Qi, *J. Phys. D-Appl. Phys.* **36** (2003) 1040.
17. J.A. Aguilar-Martínez, M.I. Pech-Canul, M. Esneider, A. Toxqui and S. Shaji, *Mater. Lett.* **78** (2012) 28.
18. H. Enoki, J. Echigoya and H. Suto, *J. Mater. Sci.* **26** (1991) 4110.
19. J.A. Aguilar-Martínez, M.A. Esneider-Alcala, M.B. Hernández, M.I. Pech Canul and S. Shaji, *J. Alloy. Compd.* **574** (2013) 278.
20. G.B. González, J.S. Okasinski, T.O. Mason, T. Buslaps and V. Honkimäki, *J. Appl. Phys*. **104** (2008) 043520.
21. N. Nadaud, N. Lequeux, M. Nanot, J. Jové and T. Roisnel, *J. Solid State Chem*. **135** (1998) 140.